

Hierarchical Spin-Polarized Nanosheet Array for Boosting Ampere-Level Water Oxidation Under Magnetic Field

Haifan Li, Quan Quan, Hongliang Dong, Yuxuan Zhang, Pengshan Xie, Dong Chen, Di Yin, Chun-Yuen Wong,* and Johnny C. Ho*

The spin-polarization strategy by manipulating magnetic electrocatalysts can promote the spin-sensitive oxygen evolution reaction (OER) while developing efficient spin-polarized materials toward ampere-level OER is still challenging. Herein, a hierarchical inter-doped (Ru-Ni)O_x nanosheet array in situ grown on nickel foam is designed, which exhibits a distinguished overpotential of 286 mV at 1 A cm⁻² under 0.4 T magnetic field and a steady lifespan of 200 h at the ampere current density (i.e., 1 A cm⁻²), outperforming most reported state-of-art spin-selective OER catalysts in alkaline electrolytes. Integrating intrinsic and interfacial spin-polarization on the inter-doped (Ru-Ni)O_x nanosheet array can significantly boost the catalytic activity for ampere-level OER under a magnetic field. Specifically, the spin-aligned Ru sites optimize the rate-determined O—O coupling step to reduce the thermodynamic barrier of OER. Meanwhile, the charge transfer kinetics is promoted due to the accelerating spin-selective electron transfer via spin pinning at the ferromagnetic-antiferromagnetic interface. The design of a hierarchical spin-polarized structure that integrates intrinsic and interfacial spin-polarization strategies provides an additional route to developing a spin-polarized OER catalyst capable of serving ampere current densities.

while generating the spin-triplet oxygen.^[2] In this regard, spin-polarized catalysts can promote spin-sensitive OER by generating the ferromagnetic exchange between intermediates and spin-aligned active sites.^[3–5] Recently, some research based on intrinsic or interfacial spin-polarization has been reported, such as high-spin ion doping,^[6] spin state modulation,^[7] interfacial ferromagnetic-antiferromagnetic (FM-AFM) coupling,^[8] and domain wall engineering.^[9] Nevertheless, developing room-temperature spin-polarized materials with a coupled ferromagnetism and metallicity has always been challenging,^[10] not to mention the additional demands on intrinsic activity and long-term durability for serving industrial OER. Therefore, proposing a new route for developing the material framework to integrate all these properties to directly break through the bottleneck of developing ampere-level spin-polarized electrocatalysts is imperative.

The construction of a hierarchical structure is a promising solution for

multifunction integration with the optimal electronic and geometric structure for superior OER performance.^[11] In contrast, using a hierarchical strategy for designing spin-polarized catalysts is rare. The chemical composition and the robust coupling effect at the interface are the cores of a highly efficient hierarchical structure, which can be designed by controlling the in situ growth of inter-doped transitional metal oxides toward

1. Introduction

Water electrolysis for hydrogen production plays a critical role in driving the transition to clean energy and achieving carbon neutrality goals.^[1] As the rate-determining pair reaction of water electrolysis, the oxygen evolution reaction (OER) is spin-sensitive owing to the spin flipping of intermediates

H. Li, C.-Y. Wong
Department of Chemistry
City University of Hong Kong
Hong Kong, SAR 999077, China
E-mail: acywong@cityu.edu.hk

Q. Quan, Y. Zhang, P. Xie, D. Chen, D. Yin, J. C. Ho
Department of Materials Science and Engineering
City University of Hong Kong
Hong Kong, SAR 999077, China
E-mail: johnnyho@cityu.edu.hk

H. Dong
Center for High Pressure Science and Technology Advanced Research
Shanghai 201203, China

H. Dong
Shanghai Key Laboratory of Material Frontiers Research in Extreme Environments
Advanced Research in Physical Sciences
Shanghai 201203, China

J. C. Ho
State Key Laboratory of Terahertz and Millimeter Waves
City University of Hong Kong
Hong Kong, SAR 999077, China

J. C. Ho
Institute for Materials Chemistry and Engineering
Kyushu University
Fukuoka 816–8580, Japan

The ORCID identification number(s) for the author(s) of this article can be found under <https://doi.org/10.1002/adfm.202420810>

DOI: 10.1002/adfm.202420810

targeted properties.^[12,13] Specifically, the doped oxides themselves can regulate the electronic structure of active adsorption sites with significant activity,^[14] long-term stability,^[15] and, particularly, spin-polarization.^[16] Additionally, the interface between the doped oxides provides abundant active sites and promotes the mass and electronic transfer to improve for enhancing OER activity at ampere-level current density^[17,18] and meanwhile lays the structural foundation for interfacial spin pinning.^[19] Noticeably, ruthenium dioxide (RuO₂) was discovered to be an itinerant antiferromagnetic material with Neel temperature (T_{Neel}) over 300 K,^[20] and this makes it an ideal platform for triggering ferromagnetic order via dilute magnetic doping, as been discovered in Mn-RuO₂.^[6,21] In contrast, nickel oxide (NiO) has stable antiferromagnetism and can, in situ, grow to form a nanosheet array by using nickel foam as a support and nickel source.^[22] Moreover, considering the positive impact of the Lorentz force and Kelvin force on O₂ bubble release, the magnetic field enhanced OER efficiency, which is expected to be more significant under higher current density.^[23] Therefore, by employing the inter-doping effect during the in situ growth of oxides on metallic foam with distinctive geometry and conductivity, it is feasible to establish a hierarchical inter-doped structure for industrial OER under a magnetic field and meanwhile integrate the intrinsic and interfacial spin-polarization effect through the doping-induced spin modulation.

Herein, a hierarchical spin-polarized inter-doped (Ru-Ni)O_x nanosheet array on nickel foam (NF) is designed, as confirmed by crystalline structure analysis and X-ray photoelectron and absorption spectroscopy. The intrinsic spin-polarization by Ni dopant into RuO₂ and interfacial FM-AFM coupling are investigated by vibrating sample magnetometer characterization. The designed (Ru-Ni)O_x@NF has an overpotential of 286 mV at 1 A cm⁻² under 0.4 T magnetic field and a steady lifespan of 200 h at 1 A cm⁻², outperforming most reported state-of-art spin-selective OER catalysts in alkaline electrolyte. Integrating intrinsic and interfacial spin-polarization on the inter-doped (Ru-Ni)O_x nanosheet array can boost the ampere-level OER catalytic activity under a magnetic field. Through in situ measurements and theoretical calculation, we found that controllably manipulating the magnetic field can not only reduce the thermodynamic barrier of the OER process by optimizing rate-determined O-O coupling step, but also promote the charge transfer kinetics via spin pinning at the ferromagnetic-antiferromagnetic interface. Designing a hierarchical structure to integrate intrinsic and interfacial spin polarization provides an additional route to develop spin-selective catalysts serving ampere-level OER.

2. Results and Discussion

2.1. Synthesis and Characterization of (Ru-Ni)O_x@NF

The hierarchical (Ru-Ni)O_x nanosheet array was synthesized by a two-step method (Figure 1a). In brief, the Ni(OH)₂ nanosheet array was in situ grown on the surface of NF with Ru-containing precursors absorbed (Figure S1, Supporting Information) by a mild hydrothermal process. After calcination, the Ru-doped NiO nanosheet array with embedded Ni-doped RuO₂ nanodomains was fabricated on NF to yield the hierarchical inter-doped (Ru-Ni)O_x nanosheet array (Figure 1b). The X-ray diffraction (XRD)

analysis was performed to study the phase composition of (Ru-Ni)O_x@NF (Figure S2, Supporting Information). The diffraction peaks associated with RuO₂, NiO, and NF without impurity phase are observed based on the standard powder diffraction files (PDF) (i.e., RuO₂ PDF#70-2662, NiO PDF#71-1179, Nickle PDF#04-0850), indicating the successful crystallization of (Ru-Ni)O_x nanosheet array on NF. Additionally, the diffraction peaks associated with specific planes of RuO₂ and NiO shift toward larger and smaller 2 θ positions compared to their 2 θ data in standard PDF (Table S1, Supporting Information). This is due to the regulation of their lattice parameters by element doping (i.e., Ru-doped NiO and Ni-doped RuO₂), which will be further discussed by crystalline and electronic structure analysis. The scanning electron microscopy (SEM) images of (Ru-Ni)O_x@NF show that (Ru-Ni)O_x nanosheets grew along the vertical direction of the NF surface to form a nanosheet array with abundant voids (Figure 1c; Figure S3, Supporting Information). Noticeably, such in situ grown nanosheet-array morphology to establish hierarchical structure can enlarge specific surface area with abundant active site exposure and enhance the mass transfer, thereby contributing to the ampere-level OER performance.^[24,25]

To further analyze the hierarchical structure of (Ru-Ni)O_x@NF, the nanosheets were ultrasonically stripped to conduct transmission electron microscopy (TEM) characterization, showcasing plentiful nanocrystals with distinct boundaries (Figure 1d). The enlarged TEM images reveal that the nanosheet is composed of Ru-doped NiO nanosheets embedded with well-dispersed Ni-doped RuO₂ nanodomains with an average diameter (D) of 4.52 nm (inset of Figure 1d; Figure S4, Supporting Information). The representative high-resolution TEM (HRTEM) image of (Ru-Ni)O_x (Figure 1e) displays clear interfaces between doped oxides (Figures S5 and S6, Supporting Information), and the interplanar distance (d) is calculated as $d = 0.3156$ nm for RuO₂ (110) and $d = 0.2105$ nm for NiO (200), respectively (Figure S7, Supporting Information). Notably, the d -spacing of RuO₂ is reduced. In contrast, the ones of NiO are increased compared to pristine RuO₂ (PDF#70-2662) and NiO (PDF#71-1179), suggesting the inter-doped feature that the Ru atoms doped into NiO nanosheets and Ni atoms doped into RuO₂ nanodomains.^[12,13,22] Moreover, the interface between doped RuO₂ and NiO can not only provide additional active sites for enhancing its OER catalytic activity but also establish a structural foundation for potential spin pinning at the interface of the inter-doped oxides.^[19] The composition of the nanosheets is also demonstrated by selected area electron diffraction (SAED, Figure 1f). The first five diffraction rings associated with various planes of RuO₂ and NiO are labeled according to the calculated interplanar distance (Figure S8, Supporting Information), and the changes in their d -spacing resulting from the inter-doping effect are in agreement with the above XRD and HRTEM analysis. The homogeneous distribution of selected elements (e.g., Ru-9%, Ni-31%, and O-60%) and the interface between inter-doped NiO and RuO₂ are shown by the energy dispersive X-ray (EDX) elemental mapping (Figure 1g; Figure S9, Supporting Information). All the results above indicate the successful formation of an inter-doped (Ru-Ni)O_x nanosheet array from the perspective of crystalline structure analysis.

To analyze the surface chemical states of the as-prepared (Ru-Ni)O_x@NF, X-ray photoelectron spectroscopy (XPS) was

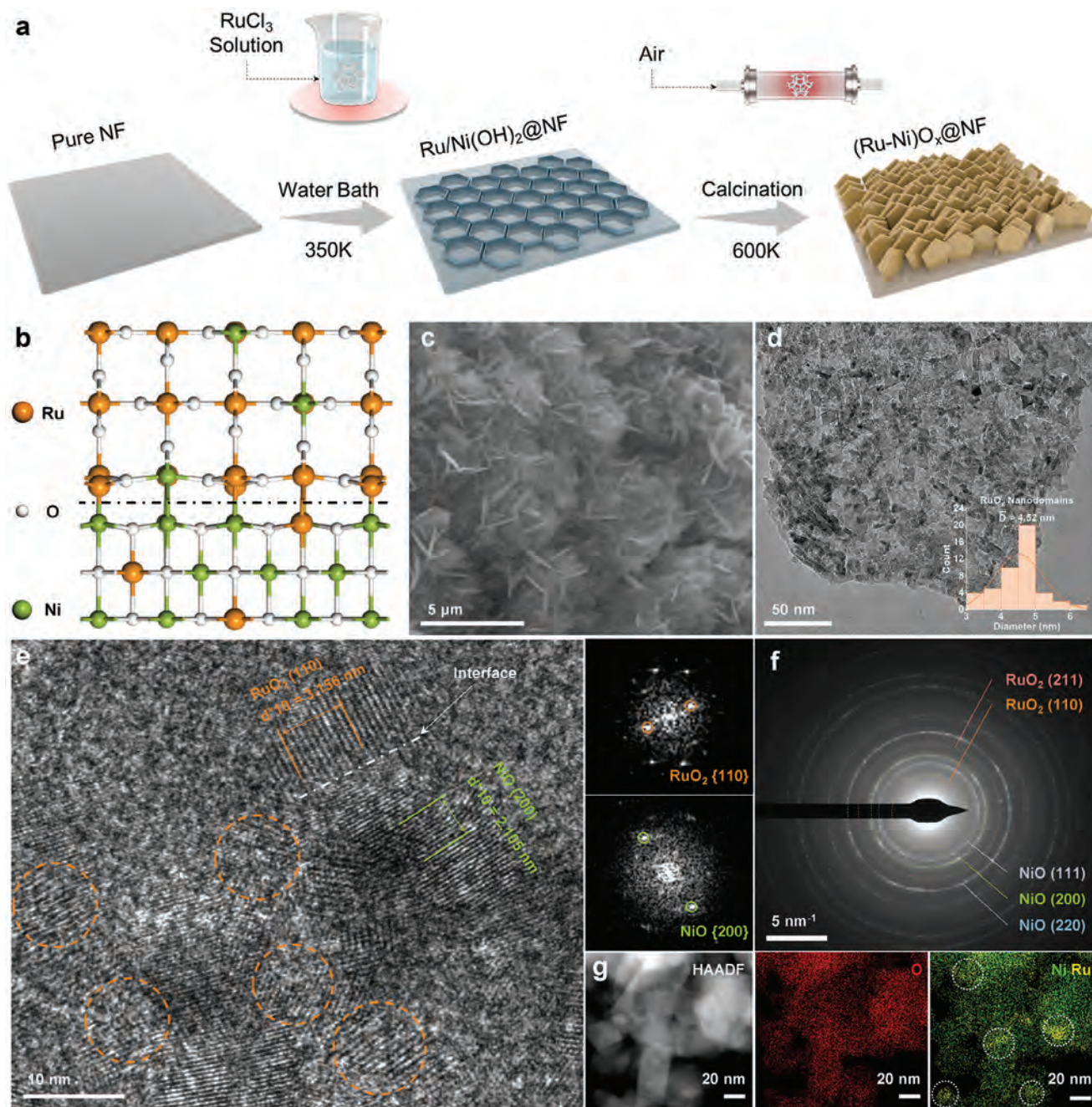


Figure 1. Synthesis and structural characterization. a) Schematic illustration of preparation of the $(\text{Ru-Ni})\text{O}_x@NF$. b) Crystal structure of the inter-doped $(\text{Ru-Ni})\text{O}_x@NF$. c) SEM image of the $(\text{Ru-Ni})\text{O}_x@NF$. d) TEM image of the $(\text{Ru-Ni})\text{O}_x$ nanosheet. Inset: diameter statistics of RuO_2 nanodomains. e) HRTEM image of the $(\text{Ru-Ni})\text{O}_x$ nanosheet and selected FFT patterns of RuO_2 and NiO . f) SAED image of the $(\text{Ru-Ni})\text{O}_x$ nanosheet. g) HAADF-STEM and EDX mapping images of the $(\text{Ru-Ni})\text{O}_x$ nanosheet.

performed for selected samples with C-1s spectra calibration (Figure S10, Supporting Information). In particular, to explore the effect of Ru element in the inter-doped $(\text{Ru-Ni})\text{O}_x$, the $\text{NiO}@NF$ was prepared as the contrast sample (Figure S11, Supporting Information) in the following analysis. The Ni-2p spectra of $\text{NiO}@NF$ and $(\text{Ru-Ni})\text{O}_x@NF$ fit with Ni-2p_{1/2} and Ni-2p_{3/2} spin-orbital peaks (Figure 2a). The shape resonance at ≈ 855 , 856, and 862 eV correspond to Ni²⁺, Ni³⁺, and their satellite peaks

of Ni-2p_{3/2}, respectively. In contrast, the ones at higher binding energy are associated with the spin-orbital peaks of Ni-2p_{1/2}.^[26] The Ni-2p peaks of $(\text{Ru-Ni})\text{O}_x@NF$ shift 0.58 eV toward higher binding energy compared to $\text{NiO}@NF$ owing to the doping effect, in which case the oxygen is more likely to receive electrons from Ni rather than Ru owing to the higher electronegativity of Ru (2.20) than Ni (1.91).^[22,27] Noticeably, the successful growth of NiO nanosheet array on NF is also supported by

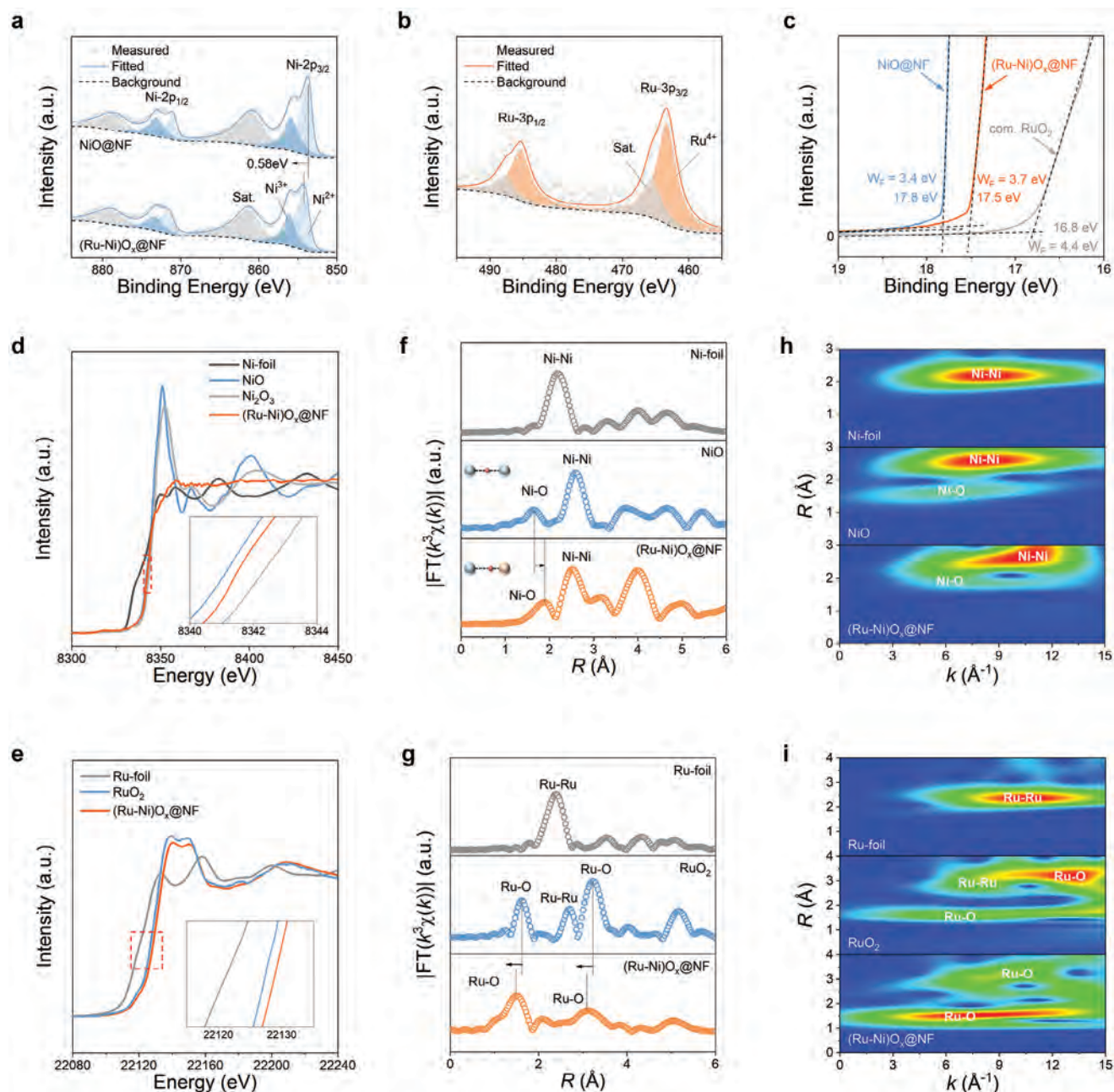


Figure 2. Surface state characterization. a) Ni-2p XPS spectra of the NiO@NF and (Ru-Ni) O_x @NF. b) Ru-3p XPS spectrum of the (Ru-Ni) O_x @NF. c) UPS spectra of the NiO@NF, (Ru-Ni) O_x @NF, and com. RuO_2 . d,e) (d) Normalized Ni K-edge XANES spectra of the Ni-foil, NiO, Ni_2O_3 , and (Ru-Ni) O_x @NF. (e) Normalized Ru K-edge XANES spectra of the Ru-foil, RuO_2 , and (Ru-Ni) O_x @NF. Inset: enlarged absorption edges image. f,g) Corresponding Fourier transform spectra. h,i) Corresponding wavelet transforms for the k^3 -weighted EXAFS signals.

comparing the Ni-2p and O-1s spectra of (Ru-Ni) O_x @NF, NiO powder and NiO@NF (Figure S12, Supporting Information). The corresponding Ru-3p spectra of (Ru-Ni) O_x @NF fit with Ru-3p $_{1/2}$ and Ru-3p $_{3/2}$ spin-orbital peaks. The shape resonance at ≈ 463 and 465 eV are marked as Ru $^{4+}$ and its satellite peaks (Figure 2b), respectively.^[13,28] The Ru $^{4+}$ is attributed to the existence of RuO_2 nanodomains embedded in NiO nanosheet array, as further indicated by the comparison of Ru-3p, Ru-3d, and O-1s spectra be-

tween commercial RuO_2 and (Ru-Ni) O_x @NF (Figure S12, Supporting Information).

To investigate the evolution of electron transport capacity for hierarchical inter-doped (Ru-Ni) O_x nanosheets, ultraviolet photoelectron spectroscopy (UPS) was applied to measure the work function (W_F) (Figure 2c). The work function of (Ru-Ni) O_x @NF is calculated to be 3.7 eV, between the 4.4 eV of commercial RuO_2 and the 3.4 eV of NiO@NF, indicating the electron

redistribution within inter-doped (Ru-Ni) O_x nanosheets because of the doping effect.^[29,30] Moreover, the lower W_F of (Ru-Ni) O_x @NF compared to RuO_2 suggests an improved carrier transport of the inter-doped nanosheets for OER. Notably, the UPS results of NiO powder and NiO@NF are analyzed to exclude the impact on W_F from the NF support and preparation process (Figure S13, Supporting Information), indicating that the construction of inter-doped nanosheets with the introduction of Ru significantly optimizes the electron transport capacity of (Ru-Ni) O_x @NF toward highly efficient electrocatalyst.

To further probe the electronic state and coordination environment of Ni and Ru atoms within the inter-doped nanosheets, the synchrotron radiation X-ray absorption fine structure (XAS) was performed for (Ru-Ni) O_x @NF. The X-ray absorption near edge structure (XANES) spectra for Ni-K Ru-K edges are shown to analyze the valence states for Ni and Ru, respectively (Figures 2d,e). The absorption edge of (Ru-Ni) O_x @NF is between NiO (Ni²⁺) and Ni₂O₃ (Ni³⁺), and the average valence state of Ni is calculated as + 2.29, while the ones of Ru is + 4.35 (inset of Figures 2d,e; Figure S14, Supporting Information), in agreement with their respective shift of binding energy shown above via XPS analysis.

The information on chemical bonds and coordination can be obtained from Fourier transform extended X-ray absorption fine structure spectroscopy (FT-EXAFS). It is observed that the two peaks at 1.90 and 2.50 Å can be attributed to Ni—O and Ni-Ni bonds (Figure 2f; Figures S15 and Table S2, Supporting Information),^[31] respectively, while the peaks at 1.50, 3.10, and 2.50 Å are associated with Ru-O and Ru-Ru bonds, accordingly (Figure 2g; Figure S16 and Table S3, Supporting Information).^[32] Notably, the average bond length of Ni-O in (Ru-Ni) O_x @NF is slightly longer than in reference NiO, while Ru—O's bond length is shorter than those of reference RuO_2 . The bond length modulation is due to the respective Ni and Ru doped into RuO_2 and NiO, which regulates the coordination environment of Ru and Ni atoms.^[27] Specifically, the higher electronegativity of Ru (2.20) than Ni (1.91) will lead to a higher affinity with oxygen and increasing charge density around Ru atoms, thereby modulating the respective bond length of Ni-O and Ru—O within the doped oxides in (Ru-Ni) O_x nanosheets, leading to the extension of Ni—O and the contraction of Ru-O.^[12] Additionally, the increasing electron density near Ru sites suggests the weakened covalency of Ru—O, and the soluble RuO_4 will be limited to production to keep the Ru elemental stable during the oxidation process, which will be discussed later.^[33] The wavelet transform-EXAFS plots further visualized chemical bond information and coordination information to support our Ni—O and Ru—O bonds analysis in the (Ru-Ni) O_x @NF sample (Figures 2h,i).

2.2. OER Performance and Magnetic Characterization

To demonstrate the potential of our designed hierarchical structure as an efficient spin-sensitive OER catalyst, a tailored electrochemical cell was built by polymethyl methacrylate (PMMA) with the switchable magnetic field applied by two magnets (Figure 3a; Figures S17 and S18, Supporting Information). The (Ru-Ni) O_x @NF prepared at 0.01 M $RuCl_3$ precursor solution is representative owing to its best catalytic activity among samples with varying Ru concentrations (Figure S19, Supporting Infor-

mation). Considering the impact on O_2 releasing from Lorentz and Kelvin forces, the intersection angle between the applying magnetic and electric fields is 90° for all the testing samples.^[23] Apart from the (Ru-Ni) O_x @NF, the NiO@NF and pure NF were also tested as references at identical conditions to discuss the mechanism of spin-polarization enhanced OER.

The linear voltammetry scanning (LSV) of the (Ru-Ni) O_x @NF, NiO@NF, and NF were tested in case of the presence and absence of a magnetic field (Figure 3b). As previously reported, a higher OER activity of the ferromagnetic NF support with the magnetic field is expected owing to the spin-aligned Ni sites.^[34] However, the NiO@NF and (Ru-Ni) O_x @NF show a larger enhancement of catalytic activity under a magnetic field, indicating their higher sensitivity to the magnetic field-induced spin alignment of active sites, which will be discussed by their intrinsic activity later. This finding is further supported by their specific overpotentials (η) at 100, 500, and 1000 mA cm⁻² (Figure S20, Supporting Information). The overpotential at 1000 mA cm⁻² with magnetic field is 286 mV for (Ru-Ni) O_x @NF, 749 for NiO@NF, and 1101 mV for NF, lower than the ones without magnetic field as 353 mV for (Ru-Ni) O_x @NF, 805 mV for NiO@NF, and 1154 mV for NF. Additionally, the decrease of η at 1000 mA cm⁻² via applying a magnetic field is the largest for (Ru-Ni) O_x @NF ($\Delta\eta$ = 67 mV), followed by NiO@NF ($\Delta\eta$ = 56 mV) and pure NF ($\Delta\eta$ = 53 mV), and this trend can also be observed at 100 and 500 mA cm⁻². The Tafel plots (Figure S21, Supporting Information) also agree with the above discussion. With the assistance of a magnetic field, all three samples show faster reaction kinetics. In particular, the (Ru-Ni) O_x @NF exhibits a Tafel slope value of 31 mV dec⁻¹, indicating its capability to be a highly efficient electrocatalyst for ampere-level OER. The influence from the direction of applying magnetic field was excluded by the LSV results under two opposite magnetic fields (Figure S22, Supporting Information).

To describe the enhancement of intrinsic OER activity for our samples with magnetic field assistance, the electrochemical active area (ECSA) tests were performed to calculate the double-layer capacitance (C_{dl}) and turnover frequency (TOF) (Table 1; Figure S23, Supporting Information). The ECSA of the (Ru-Ni) O_x @NF is significantly increased as compared to NiO@NF and NF, indicating the establishment of the hierarchical inter-doped nanosheet array can increase the specific surface area to expose a larger number of active sites (Figure S24, Supporting Information). The calculated TOF with magnetic field assistance is 3.150 s⁻¹ for (Ru-Ni) O_x @NF, 0.248 s⁻¹ for NiO@NF, and 0.071 s⁻¹ for NF, higher than the ones without magnetic field as 0.482 s⁻¹ for (Ru-Ni) O_x @NF, 0.039 s⁻¹ for NiO@NF, and 0.022 s⁻¹ for NF, respectively (Figure 3c). This observation can be explained from two aspects. On the one hand, the calculating TOF result without a magnetic field indicates that our designed (Ru-Ni) O_x @NF can not only provide more active sites owing to the larger specific surface area but also optimize the intrinsic activity of these exposed active sites, as compared to NiO@NF and NF. On the other hand, all three samples show the higher intrinsic activity by applying a magnetic field, and the changes of TOF follow the order as NF < NiO@NF < (Ru-Ni) O_x @NF. Their different sensitivity to the applying magnetic field for promoting OER can be attributed to the varying spin-polarization effect within materials, which will be discussed later.

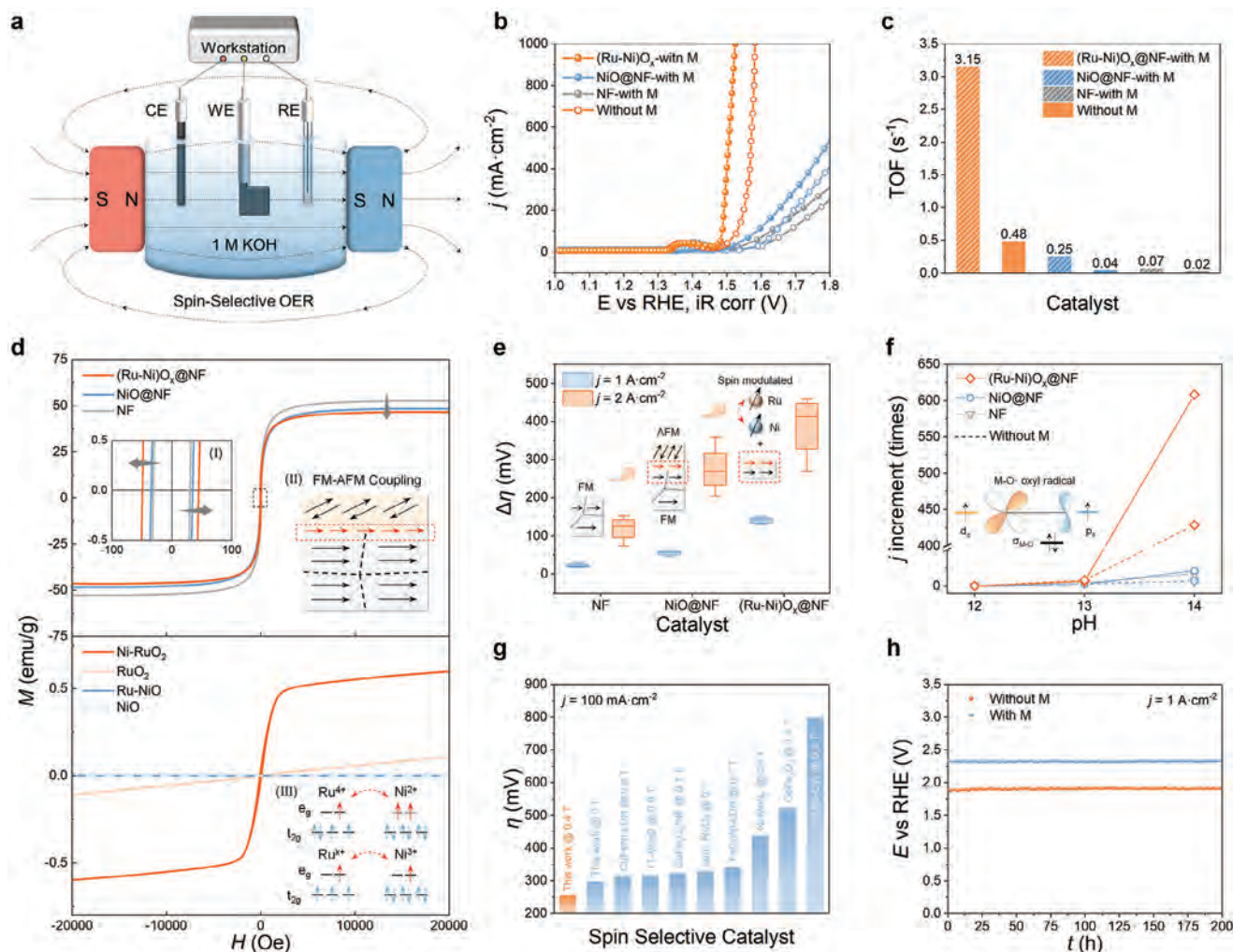


Figure 3. OER performance and magnetic characterization. a) Schematic illustration of a three-electrode system with an external magnetic field. The magnetic field at the working electrode was measured to be 398.2 mT. b) LSV curves of the (Ru-Ni) O_x @NF, NiO@NF, and NF in 1.0 M KOH and c) corresponding TOF with and without magnetic field. d) Magnetization hysteresis loops of the (Ru-Ni) O_x @NF, NiO@NF, NF, RuO $_2$, NiO, RuO $_2$ (Ni-1.3%), NiO (Ru-1.1%) at room temperature. Inset: I) Low-field region in M - H loops of the (Ru-Ni) O_x @NF, NiO@NF, and NF, II) schematic illustration of the FM-AFM coupling, and III) ferromagnetic exchange between Ru $^{4+}$ /Ru $^{3+}$ and Ni $^{2+}$ /Ni $^{3+}$. e) Changes in η at $j = 1$ and $j = 2$ A cm $^{-2}$ of the (Ru-Ni) O_x @NF, NiO@NF, and NF. f) Increment in j at 1.6 V versus RHE under various pH conditions of the (Ru-Ni) O_x @NF, NiO@NF, and NF. g) Comparison of η at $j = 100$ A cm $^{-2}$ between the (Ru-Ni) O_x @NF and the reported state-of-art spin selective OER catalysts. h) Chronopotentiometry tests (i - t) of the (Ru-Ni) O_x @NF at $j = 1$ A cm $^{-2}$.

To disclose the different spin-polarization effects among NF, NiO@NF, and (Ru-Ni) O_x @NF, the vibrating sample magnetometer (VSM) measurement was performed to study their magnetism (Figure 3d). The magnetic hysteresis (M - H) loop of the (Ru-Ni) O_x @NF, NiO@NF, and NF are shown in the top half. It is observed that the saturation moment gradually reduces in the order: (Ru-Ni) O_x @NF < NiO@NF < NF. The decrease in the saturation moment of the NiO@NF and (Ru-Ni) O_x @NF can be attributed to the in situ growth of antiferromagnetic NiO nanosheets on the ferromagnetic NF, sacrificing the overall ferromagnetism since NF is the only Ni source. In addition, the density of the grown nanosheets of (Ru-Ni) O_x @NF is greater than NiO@NF, further exacerbating the overall decline in ferromagnetism. However, the variation of coercivity is in contrast to the trend of saturation moment, and the (Ru-Ni) O_x @NF shows

the largest coercivity, followed by NiO@NF and NF (Inset I of Figure 3d). For the NiO@NF, its larger coercivity than pure NF

Table 1. The calculated C_{dl} , ECSA, and TOF of t(Ru-Ni) O_x @NF, NiO@NF, and NF (detailed in Supporting Information).

Sample	C_{dl} [mF cm $^{-2}$]	ECSA [cm 2]	TOF [s $^{-1}$]
(Ru-Ni) O_x @NF-with M	27.12	678	3.150
(Ru-Ni) O_x @NF	23.53	588	0.482
NiO@NF-with M	5.48	137	0.248
NiO@NF	4.76	119	0.039
NF-with M	5.31	133	0.071
NF	4.46	111	0.022

can be attributed to the spin pinning function at the FM-AFM interface between the NiO nanosheet and the NF support.^[8] For the (Ru-Ni)O_x@NF, the further increasing coercivity compared to NiO@NF can be discussed from two perspectives. On the one hand, this can be attributed to the higher density of nanosheet arrays on the NF support that provides more imitate FM-AFM interfaces, as discussed above by their SEM images (Figures S3 and S9, Supporting Information). On the other hand, the additional interface between doped NiO and RuO₂ within (Ru-Ni)O_x also lays the structural foundation for spin pinning to elevate coercivity. Whether there is magnetic coupling at the interface of doped oxides needs further discussion by studying the magnetism of the doped NiO and RuO₂.

To address this question, we first ultrasonically peeled the grown (Ru-Ni)O_x nanosheets from the NF support to conduct VSM measurement, and the (Ru-Ni)O_x nanosheets showed distinct ferromagnetic behaviors (Figure S25, Supporting Information). The influence from the potential debris of NF support during the ultrasonic process was excluded by the *M*–*H* loop of the NiO nanosheets peeled from NiO@NF. To further explore the source of ferromagnetism within (Ru-Ni)O_x nanosheets, a series of Ni-doped RuO₂ and Ru-doped NiO powder samples were prepared at different doping ratios with their XRD patterns and *M*–*H* loops systematically characterized (Figure S26, Supporting Information). The shift of their XRD diffraction peaks indicates the successful doping of Ru and Ni into NiO and RuO₂, respectively. Additionally, the doping level of the powder samples covers the ones of inter-doped (Ru-Ni)O_x nanosheets, as evidenced by comparing their diffraction peaks shifting, allowing us to explore the source of ferromagnetism within (Ru-Ni)O_x nanosheets via studying separate powder samples.

Four representative *M*–*H* loops of the selected samples (i.e., RuO₂, RuO₂ (Ni-1.3%), NiO (Ru-1.1%), NiO) are shown in the bottom half (Figure 3d). The Ni-doped RuO₂ shows a magnetic saturation platform while the magnetism of Ru-doped NiO remains unchanged (e.g., antiferromagnetic) compared to pure NiO powder. This can be attributed to the difference in antiferromagnetism of the pristine NiO and RuO₂. A recent study pointed out that RuO₂ has destructible itinerant antiferromagnetism. At the same time, the antiferromagnetic order within NiO is more stable,^[20] which can also be supported by the much higher Neel temperature (*T*_{Neel}) of NiO (e.g., 523 K) than RuO₂ (e.g., *T*_{Neel} ≥ 300 K). Although it is possible to induce novel ferromagnetism within NiO by defects and lattice distortion as discovered in previous research,^[35–37] the Ru dopant was unlikely to induce distinct ferromagnetism within NiO at the low doping ratio of our samples.^[38] Therefore, the doping of Ni into RuO₂ is more likely to induce the magnetism modulation than the case of Ru into NiO in the herein doping level of the powder samples and (Ru-Ni)O_x nanosheets. The exchange interaction between Ru and Ni ions is illustrated by the inset based on the Goodenough-Kanamori rule (Inset III of Figure 3d).^[39,40] In brief, Ni has half-filled spin-up *e_g* orbitals, while Ru has empty *e_g* orbitals; in this case, the virtual electron can be transferred from “half-filled to empty” so that ferromagnetism can be induced through the super exchange of FM.

Based on the above discussion, the most sensitive (Ru-Ni)O_x@NF to the spin-polarization effect for promoting OER can be attributed to the successful integration of the intrinsic

and interfacial spin-polarization strategy. On the one hand, the intrinsic spin-polarization within RuO₂ domains induced by Ni doping can provide spin-aligned Ru active sites, the intrinsic activity of which can be improved under a magnetic field. On the other hand, the more abundant interface within inter-doped nanosheets as compared to NiO@NF further amplifies the effect of FM-AFM coupling assisting spin electron transfer.

To further present the superiority of integrating intrinsic and interfacial spin-polarization for the hierarchical spin-polarized (Ru-Ni)O_x@NF toward ampere-level current density, the selected samples were tested at 1 and 2 A cm^{−2} with the circulation of the external magnetic field between 0 T and 0.4 T (Figure S27, Supporting Information). The variation of overpotential ($\Delta\eta$) was counted by the statistical method, and the $\Delta\eta$ increases in the order: NF, NiO@NF, (Ru-Ni)O_x@NF (Figure 3e). For the NiO@NF, the interface between antiferromagnetic NiO nanosheets and ferromagnetic NF enlarged the specific surface area to provide more efficient active sites and generate FM-AFM coupling to accelerate spin-selective electron transfer.^[19] Therefore, although the active sites on antiferromagnetic NiO nanosheets are not spin-polarized, the NiO@NF still exhibits the larger $\Delta\eta$ as compared to NF, which is also in agreement with the results of TOF that the NiO@NF exhibits higher enhancement in intrinsic activity than NF. For the (Ru-Ni)O_x@NF, in addition to the considerable specific surface area and several exposed active sites owing to the growth of high-density nanosheet arrays, the spin-polarization effect within Ni-doped RuO₂ provides not only efficient active sites to be spin aligned in the presence of the magnetic field, but also generate abundant FM-AFM interfaces between the doped NiO and the RuO₂ to assist spin-selective electron transfer. Therefore, integrating intrinsic and interfacial spin-polarization results in its most significant enhancement in intrinsic activity under a magnetic field compared to the NiO@NF and pure NF support.

Our claim can be further verified by the LSV results in KOH electrolytes with pH ranging from 12.0 to 14.0 (Figure S28, Supporting Information), and the increase in current density is compared (Figure 3f). It has been pointed out that the absorption of oxygen radical (O) on the spin-aligned active sites is the precondition for magnetic field enhanced OER,^[2] so the larger pH value will increase the concentration of O in the electrolyte; thus, give rise to the more significant increase of current density at the presence of magnetic field. Through this method, the degree of sensitivity of materials to spin-polarization can be described well.^[41,42] The enhancement of current density is the largest for the (Ru-Ni)O_x@NF, followed by NiO@NF and NF, indicating its superiority by simultaneously realizing intrinsic and interfacial spin polarization in a hierarchical spin-polarized framework, which amplifies the effect of magnetic field assistance. The OER catalytic activity of the (Ru-Ni)O_x@NF is further compared with other reported state-of-art spin selective OER catalysts^[7,34,43–47] by the overpotential at 100 mA cm^{−2} (Figure 3g; Table S4, Supporting Information). The (Ru-Ni)O_x@NF outperforms the selected catalysts when applying a magnetic field of 0.4 T. Moreover, the long-term stability of the (Ru-Ni)O_x@NF is also demonstrated by the chronopotentiometry (*i*–*t*) test at 1 A cm^{−2} for 200 h (Figure 3h), and the catalyst maintained robust structure in case of the presence or absence of magnetic field. The catalyst was also tested by

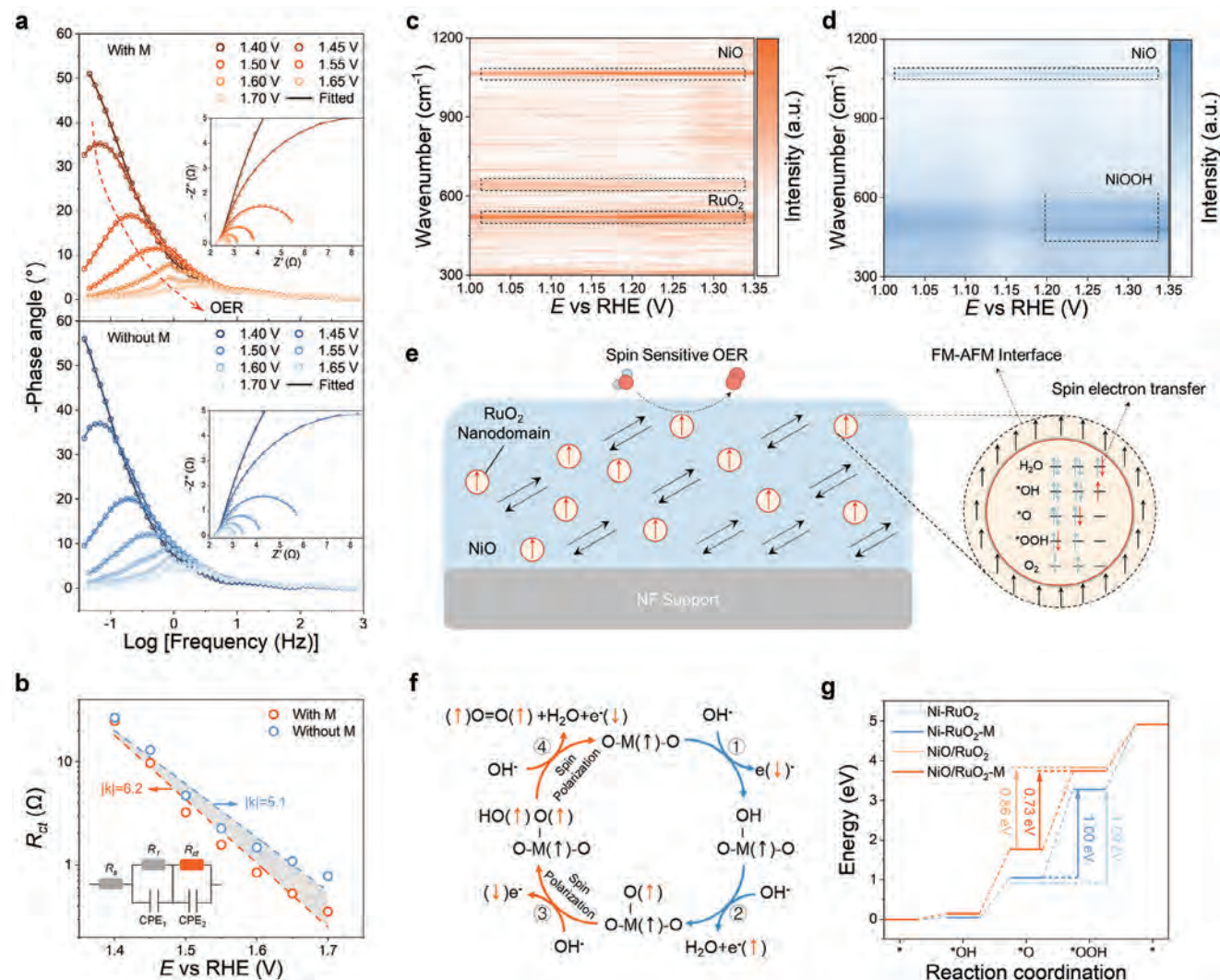


Figure 4. Operando electrochemical characterization and DFT calculation. a) Operando bode-phase plots of the (Ru-Ni)O_x@NF with and without external magnetic field. Inset: corresponding operando Nyquist plots. b) Correlation of the charge transfer resistance (R_{ct}) and applied potentials of the (Ru-Ni)O_x@NF in case of the absence and presence of the external magnetic field. Inset: electrical equivalent circuit model used for fitting R_{ct} . c,d) Contour plots of the operando Raman spectra for (c) (Ru-Ni)O_x@NF and (d) NiO@NF. e,f) Schematic illustration of (e) catalytic mechanism and (f) OER reaction pathways for (Ru-Ni)O_x@NF under magnetic field. g) The Gibbs free energy plots for Ni-doped RuO₂ and inter-doped (Ru-Ni)O_x in case of the absence and presence of the magnetic field.

anion exchange membrane water electrolysis (AEMWE) at 500 mA cm⁻² to demonstrate its potential under industrial conditions (Figure S29; Note S1, Supporting Information).

2.3. Operando Electrochemical Characterization and DFT Calculation

To verify the electron transfer assisted by magnetic field during OER, the operando electrochemical impedance spectroscopy (EIS) was tested for (Ru-Ni)O_x@NF (Figure 4a; Figure S30, Supporting Information). The high-frequency (HF) region is associated with the oxidation of the electrode interior (e.g., the appearance of NiOOH and Ruⁿ⁺, $n > 4$). In contrast, the low-frequency (LF) region is related to the OER process.^[48] No fluctuation in the

HF region can be observed for (Ru-Ni)O_x@NF owing to the stabilization of Ni and Ru atoms by forming a robust interface. A standard equivalent circuit for in situ grown hierarchical nanostructure was adapted to fit the EIS data where R_1 represents the oxidation resistance of the HF region, R_{ct} represents the charge transfer resistance of the LF region during OER, and R_s represents the solution resistance (Figure 4b).^[49] By fitting the R_{ct} as a function of applied potential, the electron transfer process is demonstrated to be more efficient by applying a magnetic field supported by the smaller R_{ct} and larger slope. As mentioned above, the FM-AFM coupling interface can help electron transfer via accelerating spin-selective electron removal on the absorption sites to lower the energy barrier of OER.^[19] In comparison, the operando EIS was also performed for NiO@NF and pure NF, respectively (Figures S31 and S32, Supporting Information). It is

observed that the FM-AFM coupling at the interface between NiO nanosheets and NF support within NiO@NF can also help accelerate spin-selective electron transfer, as revealed by the reduced R_{ct} and the increased slope while applying the magnetic field. In contrast, the impact of spin-polarization on the charge transfer of NF is limited, and only a slight reduction of R_{ct} can be observed, indicating the necessity of the FM-AFM interface for magnetic field enhanced charge transfer process. Additionally, the difference in the slopes of R_{ct} for (Ru-Ni) O_x @NF is also larger than NiO@NF, indicating the necessity of the FM-AFM coupling to the accelerating spin electron transfer under a magnetic field.

To disclose the catalytic active sites of our samples, the in situ Raman technique was employed for (Ru-Ni) O_x @NF and NiO@NF, respectively. For (Ru-Ni) O_x @NF, the shape resonance at 518 cm^{-1} (E_g), 642 cm^{-1} (A_{1g}), and 702 cm^{-1} (B_{2g}) are corresponding to the characteristic peaks of RuO_2 while the ones at 571 cm^{-1} (LO) and 1110 cm^{-1} (2LO) are related to NiO (Figure S33, Supporting Information), respectively.^[33,50] It can be seen that no obvious signal related to Ru^{n+} ($n > 4$) at ≈ 820 cm^{-1} and NiOOH can be observed owing to the stabilization of Ni and Ru atoms under the inter-doped feature (Figure 4c).^[51] In contrast to the (Ru-Ni) O_x @NF, the signal associated with NiOOH (e.g., 476 and 555 cm^{-1}) appeared at 1.20 V versus RHE in NiO@NF. It became more significant with the increasing potential (Figure 4d), indicating the NiOOH and Ru^{4+} as the real active sites of NiO@NF and (Ru-Ni) O_x @NF, respectively. This understanding can also be supported by the XPS after the OER performance test that the content of Ni^{3+} increases significantly in NiO@NF while remaining unchanged in (Ru-Ni) O_x @NF (Figure S34, Supporting Information), and the signal from Ru^{4+} is slightly reduced owing to the inevitable oxidation of Ru^{4+} . Based on the above discussion, the OER mechanism of the (Ru-Ni) O_x @NF under a magnetic field is illustrated for subsequent calculation (Figure 4e). The spin-aligned Ru^{4+} sites in Ni-doped RuO_2 nanodomains act as the active sites for spin-selective electron removal to avoid additional energy consumption for spin flipping while generating triplet oxygen to lower the energy barrier of the OER process. At the same time, the FM-AFM coupling at the interface between antiferromagnetic Ru-doped NiO and ferromagnetic Ni-doped RuO_2 nanodomains can further promote OER activity via accelerating the spin electron transfer, as proved by EIS analysis.

To theoretically verify the OER mechanism of our hierarchical spin-polarized electrocatalyst, the Ni-doped RuO_2 and inter-doped (Ru-Ni) O_x models were established for calculation (Figures S35–S37, Supporting Information). The optimal adsorption site was discussed by comparing the Gibbs free energy results with the intermediate adsorbed on different positions (Table S5, Supporting Information). The four-step method has been applied to explain the magnetic field-assisted water splitting by setting the spin-polarized direction (Figure 4f).^[6,52,53] Briefly, the spin directions of the removal electrons in the first two steps (i.e., steps ① and ②) are opposite as they come from the same p-orbit of O, as shown in Figure 4e. However, if the two removal electrons in steps ③ and ④ are spin-unaligned, additional energy consumption will be needed to perform spin flipping to generate triplet oxygen ($\uparrow O = O\uparrow$), which can be promoted by using spin-polarized materials with spin-selective functionality. The Gibbs free energy plot of OER is shown by steps (Figure 4g) follow-

ing the traditional four adsorption states marked as $*$, $*OH$, $*O$, $*OOH$ ($*$ represents the absorption site). Comparing the situation without spin-polarization, the formation of an interface between the inter-doped oxides promotes the absorption of O at the Ru site as compared to Ni-doped RuO_2 without interfacial effect, in which case the absorbate evolution can be more efficient under the limitation of linear relationship for the adsorbate evolution mechanism: $G_{*OOH} - G_{*OH} = 3.2$ eV.^[1] This understanding can also be supported by the density of states analysis that the inter-doped heterostructure leads to a more centralized hybridization between Ru-d and O-p orbitals near the Fermi level, which can lower the activation barriers for OER by increasing the total spin density to enhance the spin interaction between active sites and intermediates (Figure S38, Supporting Information).^[6,54] Further comparison of the rate-limiting step barriers of Ni-doped RuO_2 and inter-doped (Ru-Ni) O_x are shown in the absence and presence of the magnetic field. The lower variation of Gibbs free energy (ΔG) of the rate-determined step ($*O$ to $*OOH$) for both (Ru-Ni) O_x and Ni-doped RuO_2 under a magnetic field can be clearly observed, indicating the optimized O-O coupling on spin-polarized active sites that lower the thermodynamic barrier of OER.^[52] Additionally, the decreasing of ΔG with spin-polarization is more significant for (Ru-Ni) O_x than Ni-doped RuO_2 owing to the existence of the FM-AFM interface, as revealed by the above EIS analysis. The calculation result agrees with the experimental analysis that the hierarchical spin-polarized structure can serve as an efficient spin-sensitive OER catalyst by applying a magnetic field. Our hierarchical inter-doped (Ru-Ni) O_x @NF nanosheet arrays provide an additional route to developing a spin-selective OER catalyst capable of serving at ampere current densities.

3. Conclusion

In summary, a hierarchical spin-polarized (Ru-Ni) O_x nanosheet array on nickel foam is designed toward ampere-level OER under a magnetic field with the integration of intrinsic and interfacial spin-polarization. The successful growth of inter-doped (Ru-Ni) O_x nanosheets is verified through morphology and crystalline structure analysis and further substantiated by the chemical state alteration resulting from doping effects, as evidenced by XPS and XAS analyses. The intrinsic spin-polarization by Ni dopant into RuO_2 and interfacial FM-AFM coupling are proven by vibrating sample magnetometer characterization. The as-prepared (Ru-Ni) O_x @NF outperforms most reported state-of-art spin-selective OER catalysts in alkaline electrolytes; in particular, it has an overpotential of 286 mV at 1 A cm^{-2} with 0.4 T magnetic field and a steady lifespan of 200 h at 1 A cm^{-2} . Integrating intrinsic and interfacial spin-polarization on the inter-doped (Ru-Ni) O_x nanosheet array can boost the ampere-level OER activity under a magnetic field. Specifically, the thermodynamic barrier of OER is reduced under a magnetic field because the spin-aligned Ru active sites optimize the rate-determined O–O coupling step, as demonstrated by in situ experiments and theoretical calculation. Meanwhile, the charge transfer kinetics is promoted due to the spin pinning at the ferromagnetic-antiferromagnetic interface, as revealed by operando EIS analysis. The design of a hierarchical structure to integrate intrinsic and interfacial spin polarization

provides an additional route to developing a spin-polarized OER catalyst capable of serving ampere current densities.

Supporting Information

Supporting Information is available from the Wiley Online Library or from the author.

Acknowledgements

This work is supported by the City University of Hong Kong (Project no. 7020088, 9229138, 9231502, 9231539), the Shanghai Key Laboratory of Material Frontiers Research in Extreme Environments (MFree), China (No. 22dz2260800), and Shanghai Science and Technology Committee, China (No. 22JC1410300). Authors also thank the 4B9A beamline station at Beijing Synchrotron Radiation Facility (BSRF) and BL13SSW station at Shanghai Synchrotron Radiation Facility (SSRF) for the help in characterizations.

Conflict of Interest

The authors declare no conflict of interest.

Author Contributions

H.L. and Q.Q. contributed equally to this work; H.L. conceived this study; Q.Q., C.Y.W., and J.C.H. supervised the work; H.L. prepared samples, characterized the properties, and analyzed the results; Q.Q. contributed to the analysis of results; H.D. contributed to XAS characterization; Y.Z. performed the DFT calculations; P.X. revised the schematic illustration; D.C. and D.Y. provided support for sample preparation and electrochemical characterization; H.L. wrote the original manuscript assisted by Q.Q.; C. Y. W., and J.C.H.; All authors discussed the results and commented on the manuscript.

Data Availability Statement

All the necessary data have been provided in the main text and Supporting Information. Any additional information required to reanalyze the data reported in this paper is available from the corresponding author upon reasonable request.

Keywords

ampere current density, hierarchical structure, inter-doped oxide, oxygen evolution reaction, spin-polarization

Received: October 30, 2024
Revised: December 26, 2024
Published online: January 7, 2025

- [1] Z. W. Seh, J. Kibsgaard, C. F. Dickens, I. Chorkendorff, J. K. Nørskov, T. F. Jaramillo, *Science* **2017**, 355, eaad4998.
- [2] T. Wu, Z. J. Xu, *Curr. Opin. Electrochem.* **2021**, 30, 100804.
- [3] Z. Fang, W. Zhao, T. Shen, D. Qiu, Y. Lv, X. Hou, Y. Hou, *Precision Chemistry* **2023**, 1, 395.
- [4] S. Ma, Q. Fu, J. Han, T. Yao, X. Wang, Z. Zhang, P. Xu, B. Song, *Adv. Funct. Mater.* **2024**, 34, 2316544.

- [5] F. A. Garcés-Pineda, M. Blasco-Ahicart, D. Nieto-Castro, N. López, J. R. Galán-Mascarós, *Nat. Energy* **2019**, 4, 519.
- [6] L. Li, J. Zhou, X. Wang, J. Gracia, M. Valvidares, J. Ke, M. Fang, C. Shen, J. M. Chen, Y. C. Chang, C. W. Pao, S. Y. Hsu, J. F. Lee, A. Ruotolo, Y. Chin, Z. Hu, X. Huang, Q. Shao, *Adv. Mater.* **2023**, 35, 2302966.
- [7] Z. Sun, L. Lin, J. He, D. Ding, T. Wang, J. Li, M. Li, Y. Liu, Y. Li, M. Yuan, B. Huang, H. Li, G. Sun, *J. Am. Chem. Soc.* **2022**, 144, 8204.
- [8] J. Ge, R. R. Chen, X. Ren, J. Liu, S. J. H. Ong, Z. J. Xu, *Adv. Mater.* **2021**, 33, 2101091.
- [9] X. Ren, T. Wu, Z. Gong, L. Pan, J. Meng, H. Yang, F. B. Dagbjartsdottir, A. Fisher, H. J. Gao, Z. J. Xu, *Nat. Commun.* **2023**, 14, 2482.
- [10] J. Zhang, S. Shen, D. Puggioni, M. Wang, H. Sha, X. Xu, Y. Lyu, H. Peng, W. Xing, L. N. Walters, L. Liu, Y. Wang, D. Hou, C. Xi, L. Pi, H. Ishizuka, Y. Kotani, M. Kimata, H. Nojiri, T. Nakamura, T. Liang, D. Yi, T. Nan, J. Zang, Z. Sheng, Q. He, S. Zhou, N. Nagaosa, C. W. Nan, Y. Tokura, et al., *Nat. Mater.* **2024**, 23, 912.
- [11] M. Fang, G. Dong, R. Wei, J. C. Ho, *Adv. Energy Mater.* **2017**, 7, 1700559.
- [12] L. Deng, S. F. Hung, Z. Y. Lin, Y. Zhang, C. Zhang, Y. Hao, S. Liu, C. H. Kuo, H. Y. Chen, J. Peng, J. Wang, S. Peng, *Adv. Mater.* **2023**, 35, 2305939.
- [13] C. Wang, L. Qi, *Angew. Chem., Int. Ed.* **2020**, 59, 17219.
- [14] W. Zhu, F. Yao, K. Cheng, M. Zhao, C. J. Yang, C. L. Dong, Q. Hong, Q. Jiang, Z. Wang, H. Liang, *J. Am. Chem. Soc.* **2023**, 145, 17995.
- [15] W. Zhao, F. Xu, Z. Wang, Z. Pan, Y. Ye, S. Hu, B. Weng, R. Zhu, *Small* **2022**, 18, 2205495.
- [16] Y. Matsumoto, M. Murakami, T. Shono, T. Hasegawa, T. Fukumura, M. Kawasaki, P. Ahmet, T. Chikyo, S. Koshihara, H. Koinuma, *Science* **2001**, 291, 854.
- [17] Y. Hao, D. Yu, S. Zhu, C. H. Kuo, Y. M. Chang, L. Wang, H. Y. Chen, M. Shao, S. Peng, *Energy Environ. Sci.* **2023**, 16, 1100.
- [18] D. Yu, Y. Hao, S. Han, S. Zhao, Q. Zhou, C. H. Kuo, F. Hu, L. Li, H. Y. Chen, J. Ren, S. Peng, *ACS Nano* **2023**, 17, 1701.
- [19] T. Wu, X. Ren, Y. Sun, S. Sun, G. Xian, G. G. Scherer, A. C. Fisher, D. Mandler, J. W. Ager, A. Grimaud, J. Wang, C. Shen, H. Yang, J. Gracia, H. J. Gao, Z. J. Xu, *Nat. Commun.* **2021**, 12, 3634.
- [20] T. Berlijn, P. C. Snijders, O. Delaire, H. D. Zhou, T. A. Maier, H. B. Cao, S. X. Chi, M. Matsuda, Y. Wang, M. R. Koehler, P. R. C. Kent, H. H. Weitering, *Phys. Rev. Lett.* **2017**, 118, 077201.
- [21] L. Tan, X. Wu, H. Wang, J. Zeng, B. Mei, X. Pan, W. Hu, M. Faiza, Q. Xiao, Y. Zhao, C. Fu, C. Lin, X. Li, W. Luo, *ACS Catal.* **2024**, 14, 11273.
- [22] H. Zhang, Y. Lv, C. Chen, C. Lv, X. Wu, J. Guo, D. Jia, *Appl. Catal. B* **2021**, 298, 120611.
- [23] X. Li, C. Hao, Y. Du, Y. Lu, Y. Fan, M. Wang, N. Wang, R. Meng, X. Wang, Z. J. Xu, Z. Cheng, *Chin. J. Catal.* **2023**, 55, 191.
- [24] Q. Quan, Y. Zhang, F. Wang, X. Bu, W. Wang, Y. Meng, P. Xie, D. Chen, W. Wang, D. Li, C. Liu, S. Yip, J. C. Ho, *Nano Energy* **2022**, 101, 107566.
- [25] Q. Quan, X. Bu, D. Chen, F. Wang, X. Kang, W. Wang, Y. Meng, S. Yip, C. Liu, J. C. Ho, *J. Mater. Chem. A* **2022**, 10, 3953.
- [26] Y. Sun, J. Wang, Y. Qi, W. Li, C. Wang, *Adv. Sci.* **2022**, 9, 2200957.
- [27] Z. Y. Wu, F. Y. Chen, B. Li, S. W. Yu, Y. Z. Finck, D. M. Meira, Q. Q. Yan, P. Zhu, M. X. Chen, T. W. Song, Z. Yin, H. W. Liang, S. Zhang, G. Wang, H. Wang, *Nat. Mater.* **2023**, 22, 100.
- [28] D. J. Morgan, *Surf. Interface Anal.* **2015**, 47, 1072.
- [29] T. A. Shifa, F. Wang, Y. Liu, J. He, *Adv. Mater.* **2019**, 31, 1804828.
- [30] D. Yin, D. Chen, Y. Zhang, W. Wang, Q. Quan, W. Wang, Y. Meng, Z. Lai, Z. Yang, S. Yip, C. Y. Wong, X. Bu, X. Wang, J. C. Ho, *Adv. Funct. Mater.* **2023**, 33, 2303803.
- [31] M. Zhou, Y. Jiang, G. Wang, W. Wu, W. Chen, P. Yu, Y. Lin, J. Mao, L. Mao, *Nat. Commun.* **2020**, 11, 3188.
- [32] R. Yao, K. Sun, K. Zhang, Y. Wu, Y. Du, Q. Zhao, G. Liu, C. Chen, Y. Sun, J. Li, *Nat. Commun.* **2024**, 15, 2218.

- [33] D. Chen, R. Yu, K. Yu, R. Lu, H. Zhao, J. Jiao, Y. Yao, J. Zhu, J. Wu, S. Mu, *Nat. Commun.* **2024**, *15*, 3928.
- [34] Y. Ma, T. Wang, X. Sun, Y. Yao, H. Chen, G. Wu, C. Zhang, Y. Qin, *ACS Appl. Mater. Interfaces* **2023**, *15*, 7978.
- [35] I. Sugiyama, N. Shibata, Z. Wang, S. Kobayashi, T. Yamamoto, Y. Ikuhara, *Nat. Nanotechnol.* **2013**, *8*, 266.
- [36] B. Kisan, J. Kumar, S. Padmanapan, P. Alagarsamy, *Physica B* **2020**, *593*, 412319.
- [37] L. Li, X. Zhang, M. Humayun, X. Xu, Z. Shang, Z. Li, M. F. Yuen, C. Hong, Z. Chen, J. Zeng, *ACS Nano* **2023**, *18*, 1214.
- [38] A. M. Abdallah, R. Awad, *Physica B* **2022**, *629*, 413651.
- [39] J. Goodenough, A. Loeb, *Phys. Rev.* **1955**, *98*, 391.
- [40] J. Kanamori, *J. Phys. Chem. Solids* **1959**, *10*, 87.
- [41] T. Wu, J. Ge, W. Qian, R. Xiao, F. Meng, J. Wang, S. Xi, X. Wang, K. Elouarzaki, A. Fisher, Z. Xu, *Proc. Natl. Acad. Sci. U.S.A.* **2024**, *121*, e2318652121.
- [42] J. Ge, X. Ren, R. R. Chen, Y. Sun, T. Wu, S. J. H. Ong, Z. J. Xu, *Angew. Chem., Int. Ed.* **2023**, *62*, e202301721.
- [43] M. Chen, W. Zhou, K. Ye, C. Yuan, M. Zhu, H. Yu, H. Yang, H. Huang, Y. Wu, J. Zhang, X. Zheng, J. Shen, X. Wang, S. Wang, *Small* **2023**, *19*, 2300122.
- [44] L. Lin, R. Xin, M. Yuan, T. Wang, J. Li, Y. Xu, X. Xu, M. Li, Y. Du, J. Wang, S. Wang, F. Jiang, W. Wu, C. Lu, B. Huang, Z. Sun, J. Liu, J. He, G. Sun, *ACS Catal.* **2023**, *13*, 1431.
- [45] T. Sun, Z. Tang, W. Zang, Z. Li, J. Li, Z. Li, L. Cao, J. S. Dominic Rodriguez, C. O. M. Mariano, H. Xu, P. Lyu, X. Hai, H. Lin, X. Sheng, J. Shi, Y. Zheng, Y. R. Lu, Q. He, J. Chen, K. S. Novoselov, C. H. Chuang, S. Xi, X. Luo, J. Lu, *Nat. Nanotechnol.* **2023**, *18*, 763.
- [46] P. Guo, Y. Zhang, F. Han, Y. Du, B. Song, W. Wang, X. Wang, Y. Zhou, P. Xu, *J. Phys. Chem. Lett.* **2022**, *13*, 7476.
- [47] Y. Wang, Y. Shang, Z. Cao, K. Zeng, Y. Xie, J. Li, Y. Yao, W. Gan, *Chem. Eng. J.* **2022**, *439*, 135722.
- [48] H. Y. Wang, S. F. Hung, H. Y. Chen, T. S. Chan, H. M. Chen, B. Liu, *J. Am. Chem. Soc.* **2016**, *138*, 36.
- [49] Y. Lu, T. Liu, C. L. Dong, C. Yang, L. Zhou, Y. C. Huang, Y. Li, B. Zhou, Y. Zou, S. Wang, *Adv. Mater.* **2022**, *34*, 2107185.
- [50] F. Chandoul, H. Moussa, K. Jouini, A. Boukhachem, F. Hosni, M. S. Fayache, R. Schneider, *J. Mater. Sci.-Mater. El.* **2019**, *30*, 348.
- [51] Y. Zhao, M. Xi, Y. Qi, X. Sheng, P. Tian, Y. Zhu, X. Yang, C. Li, H. Jiang, *J. Energy Chem.* **2022**, *69*, 330.
- [52] X. Ren, T. Wu, Y. Sun, Y. Li, G. Xian, X. Liu, C. Shen, J. Gracia, H. J. Gao, H. Yang, Z. J. Xu, *Nat. Commun.* **2021**, *12*, 2608.
- [53] J. Chen, Y. Ling, X. Yu, G. Wang, L. Huang, A. He, Q. Fan, S. Qin, S. Xiang, M. Xu, Z. Han, J. Du, Q. Xu, *J. Alloys Compd.* **2022**, *929*, 167344.
- [54] H. Li, Y. Wang, J. Gao, V. Wang, K. Nie, F. Meng, X. Xu, Y. Jiang, N. Chen, Y. Sun, J. Chen, *J. Mater. Chem. A* **2024**, *12*, 24417.